Circular Dichroism and Magnetic Circular Dichroism Studies of the Biferrous Site of the Class Ib Ribonucleotide Reductase from *Bacillus cereus*: Comparison to the Class Ia Enzymes[†]

Ane B. Tomter,[‡,§] Caleb B. Bell III,[§,||] Åsmund K. Røhr,[‡] K. Kristoffer Andersson,*[,‡] and Edward I. Solomon*[,||]

Department of Molecular Biosciences, University of Oslo, PO Box 1041 Blindern, 0316 Oslo, Norway, and Department of Chemistry, Stanford University, 333 Campus Drive, Stanford, California 94305-5080

Received June 27, 2008; Revised Manuscript Received August 29, 2008

ABSTRACT: The rate limiting step in DNA biosynthesis is the reduction of ribonucleotides to form the corresponding deoxyribonucleotides. This reaction is catalyzed by ribonucleotide reductases (RNRs) and is an attractive target against rapidly proliferating pathogens. Class I RNRs are binuclear non-heme iron enzymes and can be further divided into subclasses. Class Ia is found in many organisms, including humans, while class Ib has only been found in bacteria, notably some pathogens. Both *Bacillus anthracis* and *Bacillus cereus* encode class Ib RNRs with over 98% sequence identity. The geometric and electronic structure of the *B. cereus* diiron containing subunit (R2F) has been characterized by a combination of circular dichroism, magnetic circular dichroism (MCD) and variable temperature variable field MCD and is compared to class Ia RNRs. While crystallography has given several possible descriptions for the class Ib RNR biferrous site, the spectroscopically defined active site contains a 4-coordinate and a 5-coordinate Fe(II), weakly antiferromagnetically coupled via μ-1,3-carboxylate bridges. Class Ia biferrous sites are also antiferromagnetically coupled 4-coordinate and 5-coordinate Fe(II), however quantitatively differ from class Ib in bridging carboxylate conformation and tyrosine radical positioning relative to the diiron site. Additionally, the iron binding affinity in *B. cereus* RNR R2F is greater than class Ia RNR and provides the pathogen with a competitive advantage relative to host in physiological, iron-limited environments. These structural differences have potential for the development of selective drugs.

Ribonucleotide reductases (RNRs[1]) catalyze the reduction of the four ribonucleotides to the corresponding deoxyribonucleotides needed for DNA synthesis and repair in all organisms (*1*−*10*). This is the first and rate limiting step in DNA biosynthesis thus making it an attractive target for drug design strategies against rapidly proliferating cells such as cancers and various pathogens (*3*). All known RNRs share a common radical-based catalytic mechanism, and three major classes are currently known (*3*−*11*). These classes appear to have a common evolutionary relationship, though they have diverged and different organisms have tuned their RNRs, via allosteric regulation, to the specific base composition of their genomes (*8*). In addition, differences in oxygen dependency and overall tertiary structures are observed across the classes (*1*−*3, 8*−*10*). Class I RNRs are iron and dioxygen dependent enzymes found in diverse species including eukaryotes, bacteria, bacteriophages, and viruses. Class II RNRs are coenzyme B_{12}-dependent, have no oxygen dependence and are found in archea, bacteria and some bacteriophages (*11*). Class III RNRs utilize a stable, but oxygen sensitive glycyl radical that only functions during anaerobiosis and are also found in archea, bacteria and bacteriophages (*1*−*3, 8, 9*).

The best studied to date is class I RNRs, which can be divided into subclasses Ia, Ib, and the recently described Ic, based on differences in allosteric regulation and primary amino acid sequence (and metal cofactor for Ic) (*12*). Most class I RNRs are composed of two similar homodimeric proteins (R1 and R2 in class Ia and Ic and R1E and R2F in class Ib). The R1 subunit contains the ribonucleotide reductase active site, and the R2 subunit houses the diiron cofactor responsible for formation of the catalytic tyrosyl radical (Y122$^{\bullet}$, using the *Escherichia coli* R2 numbering) in a four α-helix bundle characteristic of most binuclear non-heme iron enzymes (*10, 13*−*15*). The tyrosyl radical generated in the R2 subunit is transferred to the R1 subunit through a well conserved array of hydrogen bonded amino acids to form a thiyl radical in the R1 substrate binding site (*3, 8, 16*−*18*). Class Ia RNRs are expressed in all mammals, while class Ib RNRs have only been found in prokaryotes including

[†] Financial support by the Research Council of Norway # 177 661/V30 (K.K.A.), # 179513 Leiv Eiriksson travel grant (A.B.T.) and NSF-Biophysics Program Grant MCB-0342807 (E.I.S.).

* Corresponding authors. K.K.A.: e-mail, k.k.andersson@imbv.uio.no; phone, +47-22856625; fax, +47-22854443. E.I.S.: e-mail, edward.solomon@stanford.edu; phone, 650-723-9104; fax, 650-725-0259.

[‡] University of Oslo.

[||] Stanford University.

[§] These authors contributed equally to this work.

[1] Abbreviations: RNR, ribonucleotide reductase; R1, R1E, R2 and R2F, subunits of RNR; NIR, near-infrared; EPR, electron paramagnetic resonance; CD, circular dichroism; MCD, magnetic circular dichroism; VTVH MCD, variable-temperature variable-field magnetic circular dichroism; *J*, exchange coupling; 6C, 6-coordinated; 5C, 5-coordinated; 4C, 4-coordinated; SOC, spin−orbit coupling; ZFS, zero-field splitting; *D*, axial ZFS; *E*, rhombic ZFS; GS, ground state; ES, excited state; LF, ligand field.

10.1021/bi801212f CCC: $40.75
Published on Web 10/02/2008

pathogenic strains from the *Salmonella, Bacillus*, *Corynebacterium,* and *Mycobacterium* genera and are found in anaerobically grown *E. coli* cells (*19*−*24*). The only identified member of class Ic is the RNR from *Chlamydia trachomatis* which utilizes a MnFe cofactor and lacks the catalytic tyrosyl radical (*12, 25*−*27*). Despite low sequence homology across the subclasses (*28*), the amino acids that coordinate the metal sites, the tyrosyl radical (with the exception of Ic), and the amino acids in the proposed radical transport chain from R2 to R1 are conserved. Differences in pathogenic RNRs relative to human or mammalian (host) isozymes can be exploited for the treatment of diseases, thus a detailed understanding of class Ib RNRs relative to class Ia is critical. Class Ib RNRs from different pathogenic bacteria have attracted attention because of increasing resistance against existing antibiotics. Quenching of the essential tyrosyl radical is part of the action mechanism of several current RNR-targeting drugs (*3, 16, 29*).

The prototypical bacterial and mammalian class Ia enzymes are from *E. coli* and *Mus musculus* (mouse), respectively. Under conditions of DNA repair an additional R2 protein is expressed in mammalian cells (p53R2) which is induced by external agents such as the tumor suppressor p53 in response to DNA damage (*30*). p53R2 is expressed during all steps of the cell cycle for continuous deoxyribonucleotide production and is important for mitochondrial deoxyribonucleotide synthesis (*3, 31*). From crystallography and magnetic circular dichroism (MCD) spectroscopy, the biferrous sites in each of these enzymes consist of one 4-coordinate and one 5-coordinate iron center (4C+5C) (*32*−*34*). The irons are weakly antiferromagnetically coupled by two μ-1,3-carboxylate bridges with the iron coordination spheres completed by two histidine and two terminal carboxylate ligands (one monodentate to the 4C center (Fe1, which is proximal to the catalytic tyrosine) and the other bidentate to the 5C iron (Fe2)) (*33, 35, 36*). The overall crystal structure of mouse R2 is similar to *E. coli* R2, though the diiron active site in mouse R2 is more solvent accessible, shown by the ability of acetate to binds one iron during crystallization and the presence of an additional water molecule (not found in the *E. coli* crystal structure) that is H-bonded to the catalytic tyrosine (Y177 in mouse) (*37*). The 4C+5C biferrous site in R2 reacts rapidly with dioxygen to form the μ-oxo/μ-OH^- localized mixed-valent Fe(III)Fe(IV) intermediate (intermediate X) which is directly responsible for tyrosine radical generation by a proton coupled electron transfer process (*38, 39*).

The *Bacillus* genus consists of six different pathogens, including *Bacillus cereus*, the focus of this study. There is a high diversity in virulence across the *Bacillus* genus, despite close genetic relatedness (*40, 41*). *B. cereus* is a ubiquitous soil bacterium and opportunistic pathogen that is a common cause of food poisoning. The very close homologue, *B. anthracis,* causes the acute fatal disease anthrax and is a potential biological weapon due to its high toxicity (*29, 40, 42, 43*). Specific differences in the active sites of pathogenic and host RNRs could be exploited for drug design. To that end, the class Ib R2F RNR from *B. cereus* has been spectroscopically characterized.

Crystal structures of the class Ib R2F enzymes from *Salmonella typhimurium*, *Corynebacterium ammoniagenes* and *Mycobacterium tuberculosis* are currently available (*44*−*46*). No crystal structure is yet available for the *B. cereus* R2F; however, due to high sequence homology with the other class Ib enzymes (~40%) with reported crystal structures and the conservation of all catalytically important residues, it is expected to be similar (*43*). Based on crystallography, class Ib enzymes lack the pleated sheet feature present at the tip of the heart-shaped structure in the *E. coli* enzyme and more closely resemble the mammalian class Ia enzymes in this respect. The resting biferrous sites in the *S. typhimurium* and *M. tuberculosis* crystal structures are described as 4C+6C with two μ-1,3-carboxylate bridges, two histidines, two terminal carboxylates (one monodentate to the Fe1 and one bidentate to the Fe2) and a solvent derived ligand (at 2.5 and 2.4 Å, respectively) completing the coordination sphere of the 6C center (*44, 46*). The *C. ammoniagenes* structure lacks this additional water and has a 4C+5C site reminiscent of the class Ia active site structures (*45*). Also worth noting is that the catalytic Y residue is more distant from Fe1 in the class Ib enzymes (6.3 to 6.7 Å), relative to *E. coli* (~5 Å) and a water molecule fills the space between the catalytic Y residue and the dangling O of the terminal monodentate Fe1 ligand (D84 in *E. coli*) (*44*−*47*). EPR studies on the $Y^{\bullet}$ formed by class Ib R2F proteins show differences between the hyperfine tensor values of the β protons relative to the class Ia *E. coli* and mouse R2 indicating different orientations of the tyrosine ring planes (*3, 10, 16, 24, 43, 48*).

The geometric and electronic structures of the binuclear Fe(II) sites are not easily accessible through traditional spectroscopic techniques such as UV/vis absorption and electron paramagnetic resonance (EPR) (*32*). The d → d, ligand field (LF) transitions are parity forbidden, hence weak in absorption, and are in the near-IR (NIR) spectral region (5,000−16,000 cm^{-1}) which can be obscured by contributions from buffer and protein vibrations. However these transitions are intense in circular dichroism (CD) and MCD spectroscopies due to different selection rules and the inverse temperature dependence of the MCD *C*-term signal arising from a paramagnetic species (*32*). In the NIR region, CD and MCD spectroscopies probe the LF excited states of ferrous ions which reflect site geometries (*32*). Distorted six coordinate (6C) high spin ferrous ions show two characteristic transitions around 10,000 cm^{-1} split by 2,000 cm^{-1} (*49*). Five coordinate (5C) square pyramidal sites have one high-energy transition at >10,000 cm^{-1} and one low-energy transition at approximately 5000 cm^{-1}; upon rearrangement to trigonal pyramidal geometry the transition energies are decreased resulting in MCD transitions at <5,000 and <10,000 cm^{-1}. Distorted-tetrahedral (4C) sites show only low-energy LF transitions, in the 5,000 to 7,000 cm^{-1} region. Analysis of variable-temperature variable-field (VTVH) MCD data provides information on the dimer ground state (GS) splittings including the exchange coupling (*J*) which gives molecular information about ligands bridging the irons, and the axial (*D*) and rhombic (*E*) zero field splitting (ZFS) provide complementary geometric insight for each iron center.

This study utilizes a combination of NIR CD, MCD and VTVH MCD spectroscopies to obtain insight into the geometric and electronic structure of the reduced binuclear iron site in *B. cereus* R2F. NIR CD titrations were performed to obtain insight into its Fe(II) binding properties. These data

and their analyses for *B. cereus* R2F have been compared to parallel data on the previously studied class Ia RNR R2s from *E. coli* (*33*), mouse R2 (*36*), and human p53R2 (*34*) to define quantitative differences in the geometric and electronic structure of these two subclasses of binuclear iron RNRs.

EXPERIMENTAL PROCEDURES

All commercial reagents were used as obtained: pET22b plasmid (Novagen), *E. coli* BL21 (DE3), Gold cells (Stratagene), ampicillin (Sigma), ethylene diamine tetraacetic acid (EDTA) (Sigma), Bacto yeast extract (Difco), Bacto tryptone (Difco), isopropyl β-D-thiogalactopyranoside (IPTG) (Sigma), 4-(2-hydroxyethyl)-2-piperazineethanesulfonic acid (HEPES) buffer (Sigma), tris(hydroxymethyl)aminomethane (Tris) buffer (Sigma), potassium chloride (Sigma), streptomycin sulfate (Sigma), ferrous ammonium sulfate hexahydrate (Mallinckroft), DNEasy kit (Qiagen), deuterium oxide (99.9 atom % D, Aldrich), and d_3-glycerol (98 atom %, Cambridge Isotope Laboratories). Deuterated buffer was degassed with 99.9% pure argon for at least 1 h; d_3-glycerol was degassed with at least 10 freeze−pump−thaw cycles at 10^{-3} Torr.

Protein Expression and Purification. The *B. cereus* RNR R2F protein was expressed and purified as followed: Genomic DNA was isolated from the *Bacillus cereus* strain ATCC 14579 using the DNEasy kit. The coding sequence of R2F including restriction sites for *Nde*I and *Hin*dIII was amplified by PCR using the forward primer 5′- GGAATTCCATATGCGTGCGGTAAACTGG-3′ and backward primer 5′- AGGAAGCTTAAAAGTTAAACACGAAGTCATCGTC-3′. The gene was cloned into the pET22b plasmid before it was transformed into competent BL21 (DE3) Gold cells. A 10 mL overnight culture was diluted 1:100 in 1 L of Terrific Broth medium containing 100 μg/mL ampicillin and grown to an OD at 600 nm of 0.7−0.8 at 30 °C (*18*). Cultures were cooled on ice until the temperature reached 15 °C and then induced by adding IPTG to a final concentration of 1 mM. The cells were harvested after 15−16 h at 20 °C. Approximately 30 g of bacteria containing R2F was lysed utilizing an X-press (*50*) and dissolved in 100 mL of 100 mM Tris/HCl pH 7.5, with 10 mM EDTA before centrifugation. DNA was precipitated by adding streptomycin sulfate to a final concentration of 2.5% (w/v). The *B. cereus* R2F protein was precipitated with ammonium sulfate (0.26 mg/ mL). Precipitated protein was dissolved in 50 mM Tris/HCl pH 7.5 and desalted on a HiTrap desalting column (GE Healthcare) after clarification. The desalted protein solution was applied at a 2 × 5 mL HiTrap Q anion exchange column (GE Healthcare) and eluted by an 80 mL 0 to 500 mM KCl, 50 mM Tris/HCl pH 7.5, gradient. The protein was treated with 5 mM EDTA and 10 mM hydroxyurea at 4 °C for 20 min and run through a 5 mL Sephadex G25 gel filtration column, equilibrated with 50 mM deuterated buffer (50 mM HEPES, 100 mM KCl, pD = 7.9), to remove any unbound iron and reduce any radical present in the purified form. Deuterated buffer (50 mM HEPES, 100 mM KCl, pD = 7.9) was added, and the protein was concentrated to ∼4 mM. This process was repeated until the percentage of D_2O was greater than 99.9% of the solvent. The resultant solution was reconcentrated, and the protein concentration was determined using a Bradford protein assay (Bio-Rad) (*51*).

Sample Preparation. Protein samples were degassed by being rapidly purged with at least 10 vacuum/argon cycles; solid ferrous ammonimum sulfate salt was pumped at 10^{-3} kPa for at least 1 h. The protein samples were prepared and loaded into the sample holder in an inert atmosphere. A ferrous solution was made by dissolving ferrous ammonium sulfate salt in degassed deuterated buffer to a final concentration of ∼50 mM. 200 μL of the degassed apoprotein was reduced with 2 μL of 5 mM methyl viologen and 2 μL of 10 mM dithionite before the ferrous solution was added to fully load the active site and incubated for 10 min. The sample was transferred to an anaerobic cuvette for CD measurements. NIR CD spectra showed no significant change when glycerol was added to the protein sample. Protein samples were prepared for MCD studies as they were for CD, but with an additional step of mixing the protein with 50−60% (v/v) glycerol-d_3 (pD 7.8) until it was homogeneous to create an optical suitable. The samples were then immediately frozen in liquid nitrogen.

CD and MCD Instrumentation. CD studies were performed on a JASCO J200D spectropolarimeter operating with a liquid nitrogen-cooled InSb detector in the 560−2,000 nm region. Low temperature MCD and VTVH MCD data were acquired on this spectropolarimeter, modified to accommodate an Oxford Instrument SM4000-7T superconducting magnet capable of magnetic fields up to ±7.0 T and temperatures down to 1.6 K. Protein samples prepared for MCD were slowly inserted into the cryostat to reduce strain in the resulting optical glass.

Data Analysis. To find the minimum number of LF transitions required to simultaneously fit both spectra, the baseline-corrected CD and MCD spectra were fit to Gaussian band shapes using a constrained nonlinear least-squares fitting procedure. Each spectroscopic method has different selection rules, hence, transitions can have different intensities and signs but similar energies. The MCD spectra are taken at low temperature (3 K) and thus have significantly sharper bandwidths and the energies may shift by a limited amount relative to the room-temperature CD data. Thus in the analysis bands were allowed to shift by 300 cm^{-1} and widths were allowed to sharpen with decreasing temperature.

VTVH MCD data (MCD intensity data, temperature, and applied magnetic field) were fit with a non-Kramers doublet model using a simplex routine that minimized the χ^2 value using methods previously developed (*33, 52−54*). A goodness of fit parameter (χ^2/number of float parameters) was utilized to compare the different fitting results. A spin-projection model was then applied to confirm the results obtained from the doublet model and identify the specific Fe center associated with the LF transition based on the ZFS. This procedure is described in Results and Analysis.

RESULTS AND ANALYSIS

CD and Low-Temperature MCD Spectroscopy. NIR CD and MCD spectra for the fully loaded reduced *B. cereus* R2F are shown in Figure 1. The CD spectrum clearly shows one asymmetric negative high energy feature ∼10,000 cm^{-1}, one positive feature at ∼7,500 cm^{-1} and the shoulder of a lower energy positive feature. In the MCD spectrum, a positive low energy feature with a maximum at 5,800 cm^{-1} is present in addition to a broad positive feature centered at 8,000 cm^{-1}. Both spectroscopic methods have different selection rules, hence, the d → d transitions can have different intensities

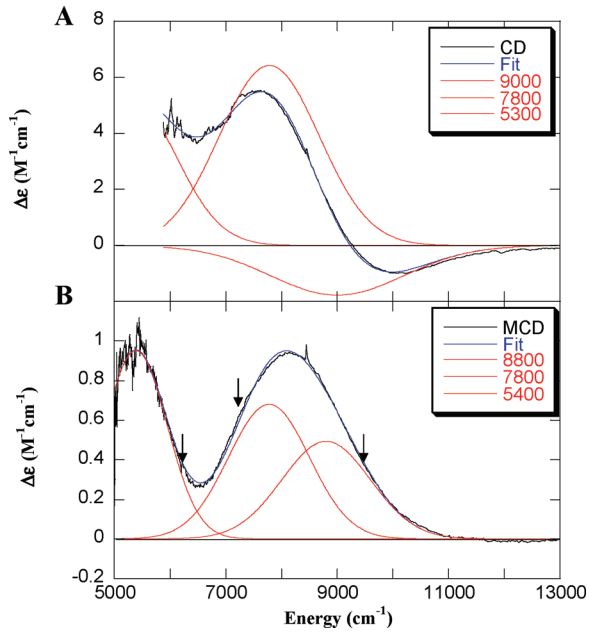

FIGURE 1: (A) CD spectrum of *B. cereus* R2F, recorded at 4 °C, and (B) MCD spectrum of *B. cereus* R2F, recorded at 3 K and 7 T. The experimental data (black line) are fit to the individual Gaussian band shapes (red line). The arrows mark where VTVH MCD data were collected.

and signs, but must have similar energies. A minimum of three transitions are required to well describe both spectra, shown in red in Figure 1. The CD spectrum, collected at 4 °C (Figure 1A), is resolved into two positive transitions at ~5,300 and ~7,800 cm^{-1} and a negative transition at ~9,000 cm^{-1} which overlaps with the 7,800 cm^{-1} feature to produce the negative asymmetric feature observed. The MCD spectrum (Figure 1B) is analogously resolved into three transitions at 5,400, 7,800 and 8,800 cm^{-1} that correlate with the CD transitions. The MCD spectrum has sharper bandwidths and slight shift in the energies, relative to the CD spectrum, because it is recorded at low temperature (~3 K). The presence of three transitions in this region requires that the two Fe(II) centers have inequivalent coordination geometries (*49*). The characteristic MCD features of a 6C iron are not observed, and thus the transition above 8,000 cm^{-1} in the CD/MCD spectra requires one of the irons to be 5C (*53*). Additionally, the presence of low energy features suggests a 4C Fe(II) is present. From the energy positions for the d → d transition in CD and MCD the *B. cereus* R2F site is tentatively assigned as 4C+5C with the two lower energy transitions arising from a 4C site and the 8,800 cm^{-1} MCD band from a 5C center for which the second transition is below the low energy detection limit of the instrument.

Ferrous iron was titrated into apo *B. cereus* R2F samples, and binding was monitored by CD spectroscopy, to estimate the binding constants and confirm the active site stoichiometry, Figures 2 and S1 in the Supporting Information. Based on a correlation to the crystal structures of other class Ib ribonucleotide reductases, the *B. cereus* R2F protein is a homodimer and each monomer can accommodate two Fe atoms. Titration curves were plotted from the CD intensity at 7,600 and 10,100 cm^{-1} (arrows in Figure 2), corresponding to the 4C and 5C site, respectively, Figure S1 in the Supporting Information. The CD intensity increases with the addition of iron and both titration curves exhibit similar

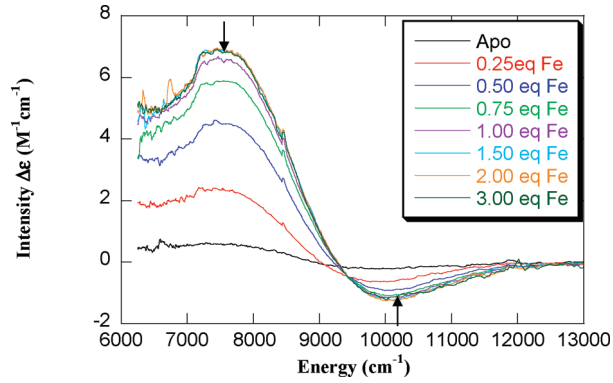

FIGURE 2: CD titration of *B. cereus* R2F with iron at 4 °C. Two equivalents of Fe is equal to a fully loaded binuclear site. The arrows show where the titration curves (Figure S1 in the Supporting Information) were plotted.

saturation behavior maximizing at ~1.5 equiv of Fe(II) per R2F monomer, where 2 equiv of Fe is equal to a fully loaded binuclear site. The equivalent saturation behavior of the CD bands indicates that the binding affinities of each individual iron site are similar and allows the binding of both metal ions to be approximated by a single binding event. Substoichiometric binding is due to partial occupancy of the active sites in the "apo" form (ICP-analysis shows that the "apo" protein contained ~0.17 equivalents of iron even after treatment with chelating agents). This shows up in CD as residual spectra (Figure 2, apo spectra) as ~10% of the fully loaded enzyme and with the same spectral shape. The titration curves corrected to the actual Fe (II) concentrations were fitted to eq 1 (*55*)

$$A = \varepsilon\{(K_d + cn + M) - [(K_d + cn + M)^2 - 4cnM]^{0.5}\}/2 \quad (1)$$

where A is the CD intensity at the selected wavelength with the corresponding absorption coefficient ε, c is the *B. cereus* R2F monomer concentration, n is the number of iron binding sites, and M is the metal ion concentration. In this CD experiment, the metal and protein concentrations are similar, thus a general form of a ligand binding equation is required. The number of binding sites (n) was included as a fit parameter and found to be 2 per monomer. This gives the binding constant ($K_b = 1/K_d$) estimated to be greater than 10^4 M^{-1} for both Fe(II) sites (Figure S1 in the Supporting Information).

Variable-Temperature Variable Field MCD. The observed MCD intensity is inversely related to the temperature confirming that these transitions are MCD *C*-terms and associated with a paramagnetic GS. Saturation magnetization data were collected at 9,310 cm^{-1} (Figure 3A), 7,190 cm^{-1} (Figure 3B) and 6,080 cm^{-1} (Figure S2 in the Supporting Information). These energies where chosen to minimize the contributions from the overlap of bands. When the MCD intensity is plotted as a function of $\beta H/2kT$, the VTVH MCD curves (isotherms) are nested, with the high-temperature data offset from the low-temperature data, indicative of rhombic ZFS of a non-Kramers doublet GS due to nonlinear field-induced mixing between the sublevels of the doublet (*56*). The observed saturation magnetization behavior at 7,190 and 9,310 cm^{-1} does not overlay (Figure 4A), suggesting that the associated transitions arise from different ferrous centers. The data collected at 6,080 cm^{-1} overlay well with the 7,190

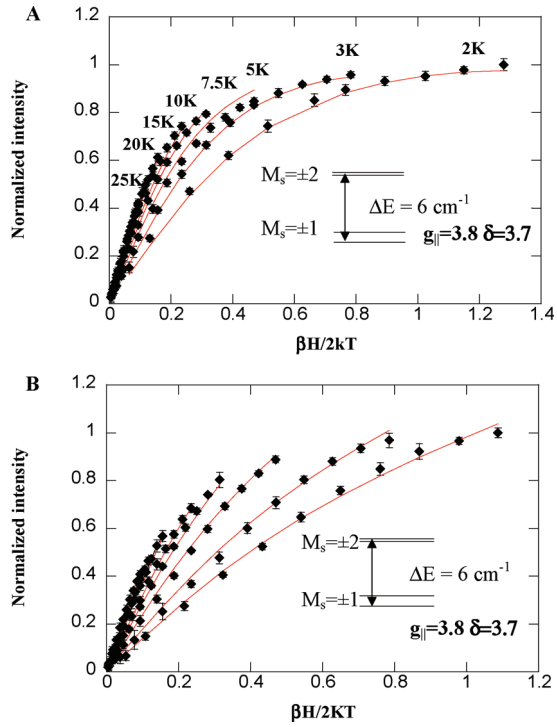

FIGURE 3: Saturation magnetization behavior of the MCD signal of *B. cereus* R2F (VTVH MCD data collected at 9,310 cm^{-1} (A) and 7,190 cm^{-1} (B) with their respected doublet fit included, red line). The intensity at one wavenumber obtained at ~1.8, 3, 5, 7.5, 10, 15, 20 and 25 K and 0, 0.35, 0.7, 1.4, 2.1, 2.8, 3.5, 4.2, 4.7, 5.6, 6.3, 7.0 T for each temperature. The data are the averaged of both positive and negative fields (to account for any field dependent baseline effects) plotted as a function of $\beta H/2kT$. Temperatures at which each isotherm was collected are shown in Figure 3A. The fit parameters are given in Table 2.

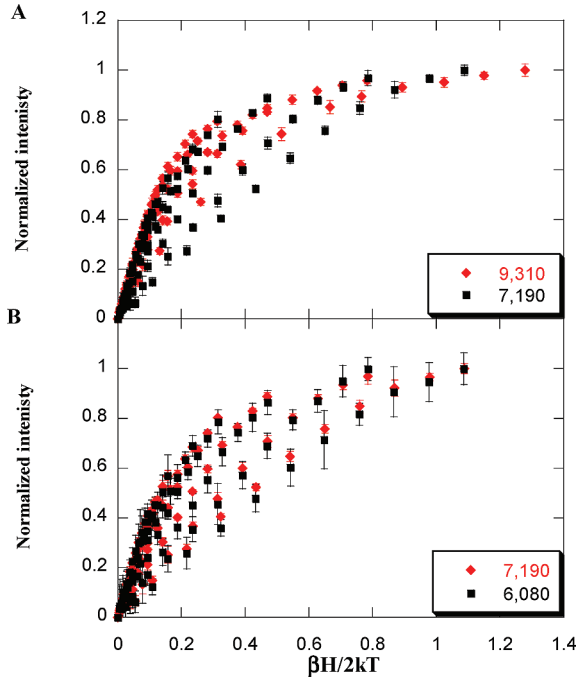

FIGURE 4: Overlay of VTVH MCD data taken at (A) 9,310 cm^{-1} (red) and 7,190 cm^{-1} (black) and (B) 7,190 cm^{-1} (red) and 6,080 cm^{-1} (black).

cm^{-1} data set (Figure 4B), however these data have a smaller signal-to-noise ratio due to interference with solvent vibrations in this energy region and were not used for the analysis below.

Table 1: Summary of VTVH MCD Parameters for the Ground and Excited States of the Reduced Binuclear Non-Heme Site for *B. cereus* R2F, *E. coli* R2 (*33*), Mouse R2 (*36*), and Human p53R2 (*34*)

	B. cereus R2F		*E. coli* R2	mouse R2	human p53R2
peak (cm^{-1})	7190	9310	7700	6250	8000
δ_1 (cm^{-1})	3.7	3.7	3.5	2.0	4.1
$g_{\|\|}$	3.8	3.8	8.0	8.0	8.0
$A_{(sat\ lim)}$	1.4	2.3	1.2	1.7	5.7
B	3.9	0.1	13.9	1.9	15.3
δ_2 (cm^{-1})	1.0	1.0	10.0	1.7	3.5
$g_{\|\|}$	8.0	8.0	4.0	4.0	4.0
$A_{(sat\ lim)}$	1.3	1.7	2.7	6.2	8.7
B	−0.1	2.3	−6.4	−5.5	4.2
energy (cm^{-1}) to first excited state	6.0	6.0	4.0	5.0	3.2

The saturation magnetization data were analyzed using a doublet model (*53*), which includes the following float parameters: ($A_{sat\ lim}$), B_i, δ_i, $g_{||}$, $g_{\perp i}$, E_i, and M_z/M_{xy} which are the *C*- and *B*-term MCD intensity, the dimer rhombic ZFS, the dimer parallel and perpendicular *g* values of the *i*th sublevel, and the energy of the *i*th level (note, the doublet GS energy is defined as zero) and the ratio of the transition polarizations in the listed directions, respectively. Initially, only a single doublet and the lowest temperature isotherm were considered. Fits to the data collected at both energies required a $g_{GS||} \cong 3.8$ and $\delta_{GS} \sim 3.7$ cm^{-1}, where a dimer $g_{||}$ value of ~4 indicates a $M_s = \pm 1$ state. Fits using $g_{||} = 8$ ($M_s = \pm 2$), 12 ($M_s = \pm 3$) or 16 ($M_s = \pm 4$) do not well describe the data sets, both graphically and based on goodness of fit parameters. In these initial fits $g_\perp$ and M_z/M_{xy} were fixed at zero, but later allowed to vary and found not to statistically improve the fit. Additional isotherms were sequentially added until the single state model could no longer reproduce the VTVH MCD data. This occurred with the inclusion of the fourth, 7.5 K temperature isotherm, and an additional excited state (ES) was added to the model. Addition of an excited doublet at ~6 cm^{-1} above the ground doublet with $g_{||} \sim 8$ well reproduced all the experimental data (up to 25 K) for both the 9,310 and 7,190 cm^{-1} data sets. Attempts to include an ES singlet or doublet with $g_{||} =$ 12 or 16 at various energies above the GS could not reproduce the magnetization behavior. The parameters obtained for fits to the entire data sets are given in the insets in Figure 3 and summarized in Table 1. Table 1 also includes the results from mouse R2, *E. coli* R2 and human p53R2 for comparison. The parameters from independent fits to both data sets are internally consistent with some variations in the *C*- and *B*-term values, as expected for a coupled biferrous system. The $M_s = \pm 1$ GS can only arise in coupled biferrous sites when the axial ZFS values (D) of each iron are oppositely signed (*vide infra*). From LF theory, 6C sites can have both positive and negative D values, however, the MCD results above rule out any 6C Fe(II). 5C trigional bipyramidal sites in proteins are typically described by $-D$ values and 4C sites by $+D$ values. From the signs of the D's required to produce the experimentally observed dimer ground and excited sublevels, the active site in *B. cereus* R2F can be assigned as 4C+5C consistent with the assignment from the energy positions of the MCD transitions (*vide supra*).

These doublets represent the energy levels of a binuclear iron site which arise from ZFS of each Fe(II) and exchange coupling between the irons in the dimer system. Deviation

Table 2: Summary of Spin-Hamiltonian Parameters for Reduced Binuclear Non-Heme *B. cereus* R2F, *E. coli* R2 (*33*), Mouse R2 (*36*), and Human p53R2 (*34*)

	B. cereus R2F				
	at 9310 cm^{-1} [a]	at 7190 cm^{-1}	*E. coli* R2 at 7700 cm^{-1}	mouse R2 at 6250 cm^{-1}	human p53R2 at 8000 cm^{-1}
J (cm^{-1})	$-2.2 < J < -1.8$	$-2.2 < J < -1.8$	$-0.65 < J < -0.3$	$-0.5 < J < 0.5$	$-0.6 < J < -0.54$
D_1 [b] (cm^{-1})	$-9 < D < -11$	$5 < D < 7$	$3 < D < 9$	$8 < D < 10$	$4 < D < 6$
E_1/D_1 (cm^{-1})	<0.1	0.33	0.33	0.23−0.33	>0
D_2 [b] (cm^{-1})	$5 < D < 7$	$-8 < D < -11$	$-11 < D < -7$	$-15 < D < -10$	$-11 < D < -8$
E_2/D_2 (cm^{-1})	0.33	<0.1	0.33	0.23−0.33	>0

[a] Indicates the energy at which the VTVH MCD data was collected and fit for extraction of parameters. [b] D_1 is assigned to the Fe(II) center associated with the d → d transition studied by VTVH MCD. In this case, D_1 (7,190 cm^{-1}) is four coordinated Fe and D_1 (9,310 cm^{-1}) is five coordinated Fe.

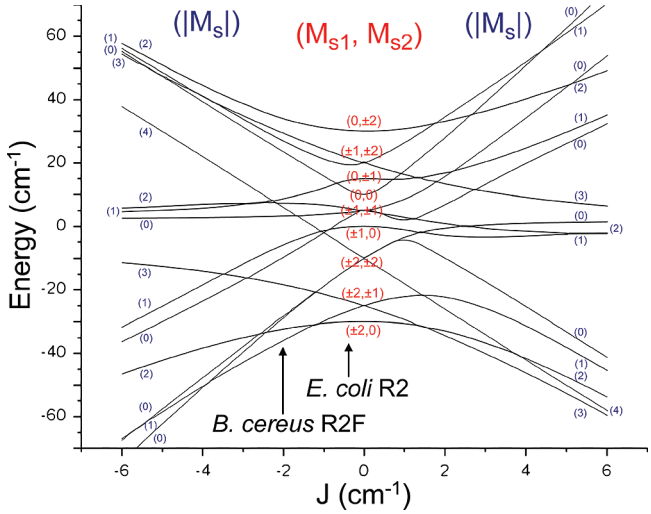

FIGURE 5: Energy level diagram of a binuclear ferrous system with $D_1 = +5$ cm^{-1} and $D_2 = -10$ cm^{-1}. The exchange coupling (J) is varied from -6 to $+6$ cm^{-1}. The right side of the diagram corresponds to a ferromagnetic interaction ($J > 0$) between the ferrous ions, and the left an antiferromagnetic interaction ($J < 0$).

from O_h or T_d symmetry in ferrous ion results in splitting of the $S = 2$ non-Kramers ions due to axial and rhombic ZFS effects, while bridging ligands will split the energy levels of the two $S = 2$ ions by J, to give $S_{tot} = 4$, 3, 2, 1 and 0 states. The combined effect is to produce 25 spin state levels. Since the exchange and ZFS terms are comparable in magnitude for binuclear ferrous systems, they need to be simultaneously considered using the appropriate spin-Hamiltonian:

$$H = -2J\hat{S}\cdot\hat{S} + D_1(\hat{S}_{z1}^2 - 1/3S(S+1)) + E_1(\hat{S}_{x1}^2 - \hat{S}_{y1}^2) + D_2(\hat{S}_{z2}^2 - 1/3S(S+1)) + E_2(\hat{S}_{x2}^2 - \hat{S}_{y2}^2) \quad (2)$$

where J is the isotropic exchange coupling between the two iron sites, and D_1, D_2, E_1, and E_2 are the axial and rhombic ZFS parameters for each iron arising from the single Fe(II) spin−orbit coupling. Different combinations of the exchange and ZFS parameters produce correlation (i.e., J/D) diagrams with different spin ladders and splitting patterns that predict different VTVH MCD behaviors (*32*). Figure 5 shows a representative energy level diagram with $D_1 = -10$ cm^{-1}, $D_2 = +5$ cm^{-1} where the ZFS tensors are assumed collinear, and $E_1 = E_2 = 0$, using the (M_{S1}, M_{S2}) notation for the wave functions when $J = 0$. Figure S4 in the Supporting Information shows the same diagram over a wider range of J values using $|S_{total}, M_{s(total)}\rangle$ notation, in the large J limit, where these are good wave functions. When J and D are comparable, the wave functions from either limit are mixed and ($|M_S|$) have been used to label the state as this expectation value determines the different VTVH MCD saturation curves, Figure 5. Noncollinearity of the ZFS tensors does not change the order of the states up to ~40 cm^{-1} (beyond the limit of the low temperature VTVH MCD experimental data), but the energy splittings are affected (*32*). The possibility of noncollinear ZFS is allowed in the analysis below where E/D can be greater than 1/3 (corresponding to a rotation of the ZFS axes). The right side of Figure 5 represents ferromagnetic coupling ($J > 0$), the center shows the uncoupled case ($J = 0$), and the left represents antiferromagnetic coupling ($J < 0$), From the doublet model analysis above, *B. cereus* R2F has a $g_{GS||} \sim 4$ and $g_{ES||} \sim 8$, i.e. the GS is $M_s = \pm 1$ and the first ES is $M_s = \pm 2$. From Figure 5, this situation occurs when the antiferromagnetic coupling is in the range of -1.0 to -2.5 cm^{-1}. Weak antiferromagnetic coupling of this magnitude is consistent with μ-1,3-carboxylate bridges.

The VTVH MCD data can be fit directly to the spin-Hamiltonian (eq 2) to extract quantitative values of the parameters and to correlate the LF transitions being studied with the individual irons through their ZFS. This complementary fitting approach uses the parameters D_1, E_1, D_2, E_2, J and the effective transition moment products M_{xy}, M_{xz}, and M_{yz} as variables to obtain the best fit (*33*). In this approach, D_1 is the Fe(II) center associated with the d → d transition studied by VTVH MCD. A variety of VTVH MCD simulations were performed to map out the solution space for the 9,310 and 7,190 cm^{-1} saturation data. From the previous results and the J/D diagram, the J-coupling was constrained to $-4 < J < 0$ and the individual iron centers were required to have opposite signed D values constrained to be less than |15 cm^{-1}| (maximum value observed in enzyme and model studies (*32*)). Figure 6A shows the best fit to the VTVH MCD data taken at 9,310 cm^{-1} on the iron assigned as 5C. These data are best described with $D_1 = -9.9$ cm^{-1}, $D_2 = +5.0$ cm^{-1} and $J = -2.2$ cm^{-1}. Additionally, the $-D$ iron required an E/D of <0.1, and the $+D$ iron is fully rhombic (E/D of ~ 0.33). Optimized spin-Hamiltonian fits with exchange of the D values (i.e., $D_1 > 0$ and $D_2 < 0$) do not accurately reproduce the data set (Figure 6C). The 7,190 cm^{-1} saturation data can be well simulated with $D_1 = +5.1$ cm^{-1}, $D_2 = -10.0$ cm^{-1} and $J = -1.8$ cm^{-1} (Figure 6B). Again, the $-D$ iron requires an E/D of <0.1 and the $+D$ iron an E/D of ~0.33. The best fit obtained switching the signs of the D's is show in Figure 6D and does not well reproduce the data. The best spin-Hamiltonian fits for the 9,310 and 7,190 cm^{-1} data sets are internally consistent, reproduce the energy spacings obtained from the doublet

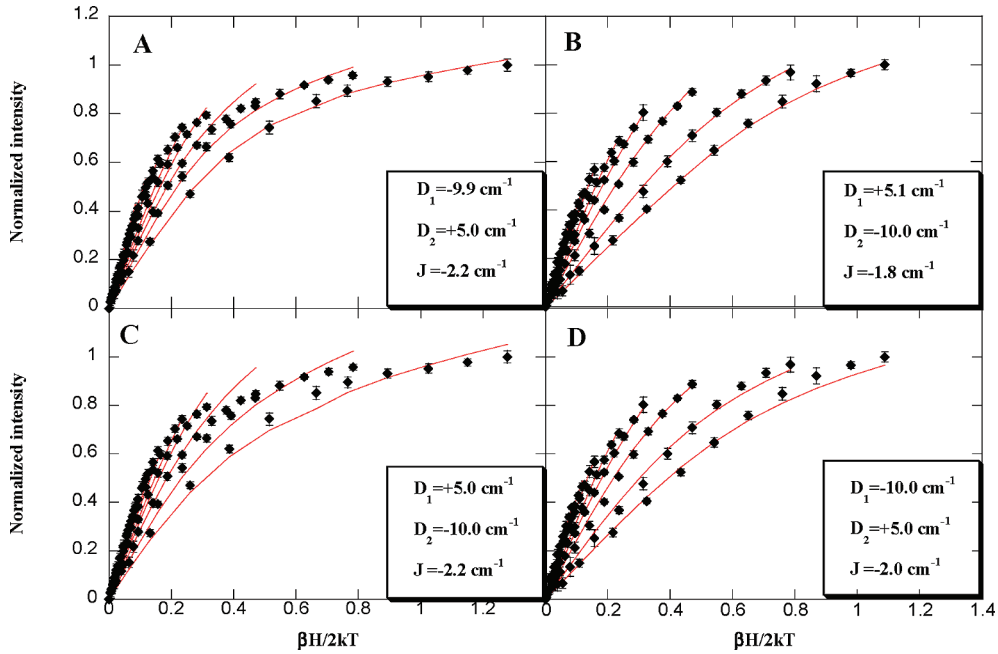

FIGURE 6: The best spin-Hamiltonian fits (red lines) using the spin projection model of *B. cereus* R2 VTVH MCD data taken at (A) 9,310 cm^{-1} and (B) 7,190 cm^{-1}. Physical parameters extracted from the data are summarized in Table 1. VTVH MCD data with the spin-Hamiltonian using the spin projection model with exchange of the *D* values at (C) 9,310 cm^{-1} and (D) 7,190 cm^{-1}.

model above and provide a detailed electronic structure description of the *B. cereus* R2F biferrous site. Table 2 summarizes the spin-Hamiltonian parameters (reported are ranges for each value that still reproduce the VTVH MCD, within experimental error) extracted from the VTVH MCD data for *B. cereus* R2F with those of *E. coli* R2, mouse R2, and human p53R2 for comparison. From this analysis the 9,310 cm^{-1} MCD transition is associated with the negative axial ZFS parameter (-9 to -11 cm^{-1}) and the 7,190 cm^{-1} transition with the $+D$ value (5 to 7 cm^{-1}). These are the 5C and 4C irons, respectively, and consistent with the above MCD assignment. From the above analyses the *B. cereus* R2F active site is best described as a 4C+5C weakly antiferromagnetically coupled ($J = -2.0 \pm 0.2$ cm^{-1}) biferrous site.

DISCUSSION

Crystallographic results on class Ib RNRs are ambiguous with respect to coordination number at the diiron active site with two of the three available structures describing the site as 4C+6C (Fe1 and Fe2, respectively, analogous to *E. coli* R2) and one as 4C+5C. The major difference between these structures is the presence of an additional water ligand saturating the coordination sphere of Fe2. CD, MCD (Figure 1) and VTVH MCD (Figure 3) results on the solution phase *B. cereus* R2F protein show that the biferrous site is 4C+5C based on the energies of the LF transitions and the signs of the *D* values associated with the transitions. We cannot rule out a water molecule present in the active site at distances greater than ~2.5 Å from Fe2 as this would not influence the ligand field of this iron, but may play a role in reactivity (i.e., access to the site, or function as a proton source in turnover) (*57*). A 4C+5C active site structure is required for the rapid $2e^-$ reduction of dioxygen bound to the site in a bridging mode, whereas a 4C+6C site would require ligand dissociation prior to dioxygen binding and electron transfer from the irons thus the reaction rate would be expected to be significantly slower.

The *B. cereus* R2F reaction rate, monitored by tyrosine radical formation, occurs at 0.2 s^{-1} (Figure S3 in the Supporting Information), which is 4 times slower than the *E. coli* R2 rate of 0.8 s^{-1} (*58*). Due to the high similarity between the spectroscopy it is likely that the structural reasons for the slower rate are not at the diiron site. One possibility is simply that the catalytic tyrosine is further away from the diiron center in the class Ib enzymes (6.8 Å relative to 4.8 Å in *E. coli* R2) and has an intervening water molecule in the H-bond network between the tyrosine and diiron site resulting in the slower overall rate (*16, 37, 44*−*47*). Alternatively, an additional water molecule near Fe2 (observed in two of the class Ib crystal structures) could slow the rate by disrupting the approach of O_2 to the site. Tyrosyl radical formation is the last step in the reaction, thus a more detailed kinetic dissection of the *B. cereus* catalytic mechanism is needed for firm insight regarding the kinetic difference, and these studies are currently underway.

VTVH MCD shows the GS of *B. cereus* R2F to be an $M_s = \pm 1$ non-Kramers doublet with an $M_s = \pm 2$ first excited doublet approximately 6 cm^{-1} above the GS. From Figure 5, this situation only arises in weakly antiferromagnetically coupled biferrous systems (with one positive and one negative *D*) and is indicative of μ-1,3 carboxylate bridges (*59*). From Figure 5, only a small increase in the strength of antiferromagnetic coupling in *B. cereus* R2F is required to interchange the ground and first excited states relative to the *E. coli* and mouse R2's. Crystallographic comparisons show one of the bridging Glu residues (E238 in *E. coli* and E267 in mouse) has changed from an anti/syn (Fe1/Fe2) asymmetric bridging mode to a more symmetric syn/anti conformation in all class Ib structures (Figure 7A shows the 4C+5C class Ib *C. ammoniagenes* R2F structure overlaid with the class Ia *E. coli* R2 structure). This altered bridging config-

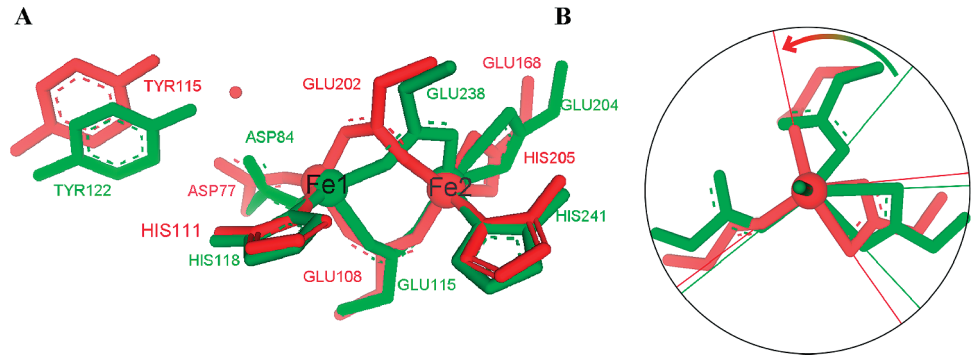

FIGURE 7: (A) Overlay of class Ia *E. coli* R2 (green, PDB ID 1PIY) with *C. ammoniagenes* R2F (red, PDB ID 1KGO). (B) This panel shows the 5C from down the Fe−N bond.

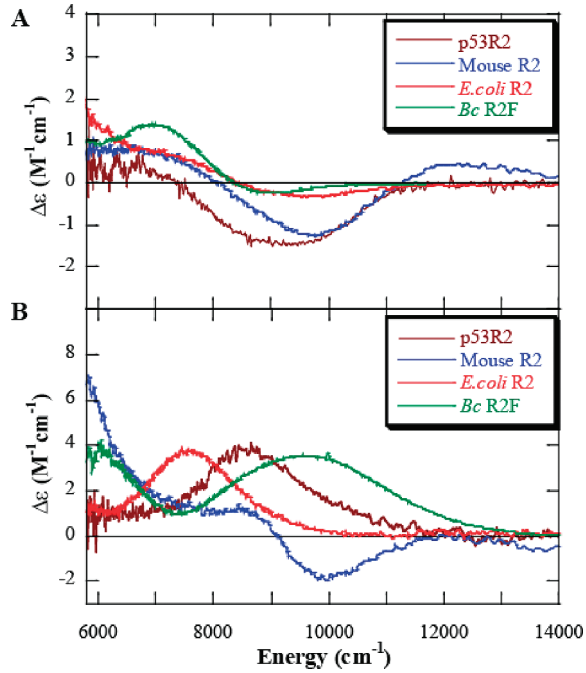

FIGURE 8: (A) CD spectra of mouse R2 (blue) (*36*), *E. coli* R2 (red) (*33*), human p53R2 (maroon) (*34*), and *B. cereus* R2F (green) recorded at 4 °C. (B) MCD spectra of mouse R2 (blue) (*36*), *E. coli* R2 (red) (*33*), human p53R2 (maroon) (*34*), and *B. cereus* R2F (green) recorded at 1.6 K and 7 T.

Table 3: Summary of the Ligand-Field Transition Energies from CD and MCD Gaussian Resolution Analysis for Reduced Binuclear Non-Heme Ribonucleotide Reductase from *B. cereus* R2F, *E. coli* R2 (*33*), Mouse R2 (*36*), and Human p53R2 (*34*)

	B. cereus R2F	*E. coli* R2	mouse R2	human p53R2
CD	5300 (+)	5500 (+)	5600 (+)	5600 (+)
	7800 (+)	7000 (+)	6700 (+)	8250 (−)
	9000 (−)	9700 (−)	9600 (−)	9500 (−)
MCD	5400 (+)	5200 (+)	5500 (+)	5700 (+)
	7800 (+)	7400 (+)	6800 (+)	8100 (+)
	8800 (+)	9100 (−)[a]	10000 (−)	9500 (+)

[a] The peak at 9100 cm^{-1} is seen at low Fe(II) concentration.

uration appears to increase the overlap of the magnetic orbitals involved in superexchange resulting in the experimentally observed strengthening of the antiferromagnetic coupling in *B. cereus* R2F relative to class Ia RNRs.

Figure 8 and Table 3 compare the CD/MCD results for *B. cereus* R2F with three class Ia R2 enzymes (*33*−*36*). The energy positions of the transitions are very similar, with *B. cereus* R2F and *E. coli* R2 being the most similar. However the sign of the highest energy MCD transition (assigned to the 5C iron) is positive in *B. cereus* R2F and p53R2 but negative in *E. coli* and mouse R2. This reflects structural differences at Fe2. Most high-spin ferrous sites show all positive MCD *C*-term signals due to the lack of spin−orbit coupling between the d_σ excited states (i.e., there is no spin−orbit matrix element coupling the d_{z^2} and $d_{x^2-y^2}$ orbitals). The negative feature observed for the higher energy transition in *E. coli* R2 likely results from mixing of some of the d_π GS into the excited d_σ orbitals through a rhombic distortion of the ligand field. This mixing allows components of the ES to spin−orbit couple to produce equal and opposite MCD signals for the transtions to the two LF excited states, hence the negative MCD intensity of the 9,000 cm^{-1} band in *E. coli* and mouse R2, Figure 8, red and blue (*49*). The observation that this feature is positive in *B. cereus* R2F (Figure 8, green) requires that its 5C site is more axial than the 5C site in *E. coli* and mouse R2. Indeed, VTVH MCD data show that the *B. cereus* R2F 5C iron is more axial ($E/D < 0.1$) relative to *E. coli* or mouse R2 ($E/D \sim 0.33$), Table 2 (*32, 35, 37*). This is consistent with the crystal structures; looking down the Fe2−N bond (Figure 7B) the class Ib enzymes more closely approach an idealized square pyramidal geometry (arrow in Figure 7B) than the class Ia R2's. Fe2 is less rhombically distorted in class Ib due to both the closer terminal bidentate carboxylate and alteration of the bridging carboxylate mode. An interesting final note is that the iron binding behavior observed for *B. cereus* R2F is more similar to that of *E. coli* R2 (strong noncooperative binding) relative to the observed cooperative binding in mouse R2 (*33, 36*). This higher iron binding affinity would give the pathogen a competitive advantage relative to the host and under physiological, iron-limited conditions.

This study experimentally describes the electronic and geometric structure of the solution phase reduced binuclear active site of *B. cereus* R2F a class Ib RNR and correlates it to the *E. coli*, mouse and p53 R2 subunits. Quantitative differences in pathogenic RNRs relative to host can be exploited for selective therapies against infections. *B. anthracis* R2F is sensitive to radical scavengers, such as *N*-hydroxylamines, and these have been suggested for use in combination therapies (*43*). Also, there is a remarkable difference between *B. cereus* and *B. anthracis* R2F relative to *E. coli* R2 in the sensitivity toward the radical scavenger, hydroxyurea with *E. coli* growth more strongly inhibited. Thus drug designs exploiting differences in pathogenic relative to host (i.e., class Ib vs class Ia) active site structures, such as described above, should be explored.

ACKNOWLEDGMENT

We thank Professor Anne-Brit Kolsto (University of Oslo, Oslo, Norway) for generously providing us the *B. cereus* strains.

SUPPORTING INFORMATION AVAILABLE

Fits to the CD titrations and VTVH MCD data collected at 6080 cm^{-1}. This material is available free of charge via the Internet at http://pubs.acs.org.

REFERENCES

1. Jordan, A., and Reichard, P. (1998) Ribonucleotide reductases. *Annu. Rev. Biochem. 67*, 71–98.
2. Reichard, P. (1993) From RNA to DNA, Why So Many Ribonucleotide Reductases. *Science 260*, 1773–1777.
3. Andersson, K. K. (Ed.) (2008) *Ribonucleotide reductase*, Nova Science publishers, Inc., Hauppauge, NY.
4. Ashley, G. W., and Stubbe, J. (1985) Current Ideas on the Chemical Mechanism of Ribonucleotide Reductases. *Pharmacol. Ther. 30*, 301–329.
5. Stubbe, J. A., and Ackles, D. (1980) On the Mechanism of Ribonucleoside Diphosphate Reductase from *Escherichia coli* - Evidence for 3′-C-H Bond-Cleavage. *J. Biol. Chem. 255*, 8027–8030.
6. Stubbe, J. A. (1990) Ribonucleotide Reductases - Amazing and Confusing. *J. Biol. Chem. 265*, 5329–5332.
7. Stubbe, J. (1990) Ribonucleotide Reductases. *Adv. Enzymol. Relat. Areas Mol. Biol. 63*, 349–419.
8. Eklund, H., Uhlin, U., Farnegardh, M., Logan, D. T., and Nordlund, P. (2001) Structure and function of the radical enzyme ribonucleotide reductase. *Prog. Biophys. Mol. Biol. 77*, 177–268.
9. Nordlund, N., and Reichard, P. (2006) Ribonucleotide reductases. *Annu. Rev. Biochem. 75*, 681–706.
10. Andersson, K. K., and Graslund, A. (1995) Diiron-oxygen proteins. *Adv. Inorg. Chem. 43*, 359–408.
11. Stubbe, J. A. (1983) Mechanism of B12-Dependent Ribonucleotide Reductase. *Mol. Cell. Biochem. 50*, 25–45.
12. Hogbom, M., Stenmark, P., Voevodskaya, N., McClarty, G., Graslund, A., and Nordlund, P. (2004) The radical site in chlamydial ribonucleotide reductase defines a new R2 subclass. *Science 305*, 245–248.
13. Sjoberg, B. M., Graslund, A., and Eckstein, F. (1983) A Substrate Radical Intermediate in the Reaction between Ribonucleotide Reductase from *Escherichia coli* and 2′-Azido-2′-Deoxynucleoside Diphosphates. *J. Biol. Chem. 258*, 8060–8067.
14. Tong, W. H., Chen, S., Lloyd, S. G., Edmondson, D. E., Huynh, B. H., and Stubbe, J. (1996) Mechanism of assembly of the diferric cluster-tyrosyl radical cofactor of *Escherichia coli* ribonucleotide reductase from the diferrous form of the R2 subunit. *J. Am. Chem. Soc. 118*, 2107–2108.
15. Bollinger, J. M., Tong, W. H., Ravi, N., Huynh, B. H., Edmondson, D. E., and Stubbe, J. (1995) Use of Rapid Kinetics Methods to Study the Assembly of the Diferric-Tyrosyl Radical Cofactor of *Escherichia coli* Ribonucleotide Reductase. *Methods Enzymol. 258*, 278–303.
16. Kolberg, M., Strand, K. R., Graff, P., and Andersson, K. K. (2004) Structure, function, and mechanism of ribonucleotide reductases. *Biochim. Biophys. Acta 1699*, 1–34.
17. Sjoberg, B. M. (1997) Ribonucleotide reductases - A group of enzymes with different metallosites and a similar reaction mechanism. *Struct. Bonding (Berlin) 88*, 139–173.
18. Rova, U., Goodtzova, K., Ingemarson, R., Behravan, G., Graslund, A., and Thelander, L. (1995) Evidence by Site-Directed Mutagenesis Supports Long-Range Electron-Transfer in Mouse Ribonucleotide Reductase. *Biochemistry 34*, 4267–4275.
19. Jordan, A., Gibert, I., and Barbe, J. (1994) Cloning and Sequencing of the Genes from *Salmonella typhimurium* Encoding a New Bacterial Ribonucleotide Reductase. *J. Bacteriol. 176*, 3420–3427.
20. Jordan, A., Pontis, E., Aslund, F., Hellman, U., Gibert, I., and Reichard, P. (1996) The ribonucleotide reductase system of *Lactococcus lactis* - Characterization of an nrdEF enzyme and a new electron transport protein. *J. Biol. Chem. 271*, 8779–8785.
21. Scotti, C., Valbuzzi, A., Perego, M., Galizzi, A., and Albertini, A. M. (1996) The *Bacillus subtilis* genes for ribonucleotide reductase are similar to the genes for the second class I NrdE/NrdF enzymes of *Enterobacteriaceae*. *Microbiology 142*, 2995–3004.
22. Yang, F. D., Lu, G. Z., and Rubin, H. (1994) Isolation of Ribonucleotide Reductase from *Mycobacterium tuberculosis* and Cloning, Expression, and Purification of the Large Subunit. *J. Bacteriol. 176*, 6738–6743.
23. Jordan, A., Pontis, E., Atta, M., Krook, M., Gibert, I., Barbe, J., and Reichard, P. (1994) A 2nd Class-I Ribonucleotide Reductase in Enterobacteriaceae - Characterization of the *Salmonella-Typhimurium* Enzyme. *Proc. Natl. Acad. Sci. U.S.A. 91*, 12892–12896.
24. Allard, P., Barra, A. L., Andersson, K. K., Schmidt, P. P., Atta, M., and Graslund, A. (1996) Characterization of a new tyrosyl free radical in *Salmonella typhimurium* ribonucleotide reductase with EPR at 9.45 and 245 GHz. *J. Am. Chem. Soc. 118*, 895–896.
25. Voevodskaya, N., Lendzian, F., Ehrenberg, A., and Graslund, A. (2007) High catalytic activity achieved with a mixed manganese-iron site in protein R2 of Chlamydia ribonucleotide reductase. *FEBS Lett. 581*, 3351–3355.
26. Jiang, W., Bollinger, J. M., and Krebs, C. (2007) The active form of *Chlamydia trachomatis* ribonucleotide reductase R2 protein contains a heterodinuclear Mn(IV)/Fe(III) cluster with S=1 ground state. *J. Am. Chem. Soc. 129*, 7504.
27. Jiang, W., Yun, D., Saleh, L., Barr, E. W., Xing, G., Hoffart, L. M., Maslak, M. A., Krebs, C., and Bollinger, J. M. (2007) A manganese(IV)/iron(III) cofactor in *Chlamydia trachomatis* ribonucleotide reductase. *Science 316*, 1188–1191.
28. Thelander, L., and Graslund, A. (1994) Ribonucleotide Reductase in Mammalian Systems. *Met. Ions Biol. Syst. 30*, 109–129.
29. Lassmann, G., Thelander, L., and Graslund, A. (1992) Epr Stopped-Flow Studies of the Reaction of the Tyrosyl Radical of Protein-R2 from Ribonucleotide Reductase with Hydroxyurea. *Biochem. Biophys. Res. Commun. 188*, 879–887.
30. Tanaka, H., Arakawa, H., Yamaguchi, T., Shiraishi, K., Fukuda, S., Matsui, K., Takei, Y., and Nakamura, Y. (2000) A ribonucleotide reductase gene involved in a p53-dependent cell-cycle checkpoint for DNA damage. *Nature 404*, 42–49.
31. Pontarin, G., Ferraro, P., Hakansson, P., Thelander, L., Reichard, P., and Bianchi, V. (2007) p53R2-dependent ribonucleotide reduction provides deoxyribonucleotides in quiescent human fibroblasts in the absence of induced DNA damage. *J. Biol. Chem. 282*, 16820–16828.
32. Solomon, E. I., Brunold, T. C., Davis, M. I., Kemsley, J. N., Lee, S. K., Lehnert, N., Neese, F., Skulan, A. J., Yang, Y. S., and Zhou, J. (2000) Geometric and electronic structure/function correlations in non-heme iron enzymes. *Chem. Rev. 100*, 235–349.
33. Yang, Y. S., Baldwin, J., Ley, B. A., Bollinger, J. M., and Solomon, E. I. (2000) Spectroscopic and electronic structure description of the reduced binuclear non-heme iron active site in ribonucleotide reductase from *E. coli*: Comparison to reduced Delta(9) desaturase and electronic structure contributions to differences in O-2 reactivity. *J. Am. Chem. Soc. 122*, 8495–8510.
34. Wei, P. P., Tomter, A. B., Rohr, A. K., Andersson, K. K., and Solomon, E. I. (2006) Circular dichroism and magnetic circular dichroism studies of the active site of p53R2 from human and mouse: Iron binding and nature of the biferrous site relative to other ribonucleotide reductases. *Biochemistry 45*, 14043–14051.
35. Pulver, S. C., Tong, W. H., Bollinger, J. M., Stubbe, J., and Solomon, E. I. (1995) Circular dichroism and magnetic circular dichroism studies of the fully reduced binuclear non-heme iron active site in the *Escherichia coli* R2 subunit of ribonucleoside diphosphate reductase. *J. Am. Chem. Soc. 117*, 12664–12678.
36. Strand, K. R., Yang, Y. S., Andersson, K. K., and Solomon, E. I. (2003) Circular dichroism and magnetic circular dichroism studies of the biferrous form of the R2 subunit of ribonucleotide reductase from mouse: Comparison to the R2 from *Escherichia coli* and other binuclear ferrous enzymes. *Biochemistry 42*, 12223–12234.
37. Strand, K. R., Karlsen, S., Kolberg, M., Rohr, A. K., Gorbitz, C. H., and Andersson, K. K. (2004) Crystal structural studies of changes in the native dinuclear iron center of ribonucleotide reductase protein R2 from mouse. *J. Biol. Chem. 279*, 46794–46801.
38. Burdi, D., Willems, J. P., Riggs-Gelasco, P., Antholine, W. E., Stubbe, J., and Hoffman, B. M. (1998) The Core Structure of X Generated in the Assembly of the Diiron Cluster of Ribonucleotide Reductase: 17O2 and H217O ENDOR. *J. Am. Chem. Soc. 120*, 12910–12919.
39. Mitic, N., Clay, M. D., Saleh, L., Bollinger, J. M., and Solomon, E. I. (2007) Spectroscopic and electronic structure studies of intermediate X in ribonucleotide reductase R2 and two variants:

A description of the Fe-IV-Oxo bond in the Fe-III-O-Fe-IV dimer. *J. Am. Chem. Soc. 129*, 9049–9065.
40. Helgason, E., Okstad, O. A., Caugant, D. A., Johansen, H. A., Fouet, A., Mock, M., Hegna, I., and Kolsto, A. B. (2000) *Bacillus anthracis*, *Bacillus cereus*, and *Bacillus thuringiensis*-one species on the basis of genetic evidence. *Appl. Environ. Microbiol. 66*, 2627–2630.
41. Tourasse, N. J., Helgason, E., Okstad, O. A., Hegna, I. K., and Kolsto, A. B. (2006) The *Bacillus cereus* group: novel aspects of population structure and genome dynamics. *J. Appl. Microbiol. 101*, 579–593.
42. Ehling-Schulz, M., Fricker, M., and Scherer, S. (2004) *Bacillus cereus*, the causative agent of an emetic type of food-borne illness. *Mol. Nutr. Food. Res. 48*, 479–487.
43. Torrents, E., Sahlin, M., Biglino, D., Graslund, A., and Sjoberg, B. M. (2005) Efficient growth inhibition of *Bacillus anthracis* by knocking out the ribonucleotide reductase tyrosyl radical. *Proc. Natl. Acad. Sci. U.S.A. 102*, 17946–17951.
44. Eriksson, M., Jordan, A., and Eklund, H. (1998) Structure of *Salmonella typhimurium* nrdF ribonucleotide reductase in its oxidized and reduced forms. *Biochemistry 37*, 13359–13369.
45. Hogbom, M., Huque, Y., Sjoberg, B. M., and Nordlund, P. (2002) Crystal structure of the di-iron/radical protein of ribonucleotide reductase from *Corynebacterium ammoniagenes*. *Biochemistry 41*, 1381–1389.
46. Uppsten, M., Davis, J., Rubin, H., and Uhlin, U. (2004) Crystal structure of the biologically active form of class 1b ribonucleotide reductase small subunit from *Mycobacterium tuberculosis*. *FEBS Lett. 569*, 117–122.
47. Logan, D. T., Su, X. D., Aberg, A., Regnstrom, K., Hajdu, J., Eklund, H., and Nordlund, P. (1996) Crystal structure of reduced protein R2 of ribonucleotide reductase: The structural basis for oxygen activation at a dinuclear iron site. *Structure 4*, 1053–1064.
48. Andersson, K. K., Schmidt, P. P., Katterle, B., Strand, K. R., Palmer, A. E., Lee, S. K., Solomon, E. I., Graslund, A., and Barra, A. L. (2003) Examples of high-frequency EPR studies in bioinorganic chemistry. *J. Biol. Inorg. Chem. 8*, 235–247.
49. Pavel, E. G., Kitajima, N., and Solomon, E. I. (1998) Magnetic circular dichroism spectroscopic studies of mononuclear non-heme ferrous model complexes. Correlation of excited- and ground-state electronic structure with geometry. *J. Am. Chem. Soc. 120*, 3949–3962.
50. Magnusson, K. E., and Edebo, L. (1976) Influence of cell concetration, temperature, and press performance on flow characteristics and disintegration in freeze-pressing of *Saccharomyces cerevisiae* with X-press. *Biotechnol. Bioeng. 18*, 865–883.
51. Bradford, M. M. (1976) Rapid and Sensitive Method for Quantitation of Microgram Quantities of Protein Utilizing Principle of Protein-Dye Binding. *Anal. Biochem. 72*, 248–254.
52. Wei, P. P., Skulan, A. J., Mitic, N., Yang, Y. S., Saleh, L., Bollinger, J. M., and Solomon, E. I. (2004) Electronic and spectroscopic studies of the non-heme reduced binuclear iron sites of two ribonucleotide reductase variants: Comparison to reduced methane monooxygenase and contributions to O-2 reactivity. *J. Am. Chem. Soc. 126*, 3777–3788.
53. Solomon, E. I., Pavel, E. G., Loeb, K. E., and Campochiaro, C. (1995) Magnetic Circular-Dichroism Spectroscopy as a Probe of the Geometric and Electronic-Structure of Nonheme Ferrous Enzymes. *Coord. Chem. Rev. 144*, 369–460.
54. Neese, F., and Solomon, E. I. (1847) (1999) MCD C-term signs, saturation behavior, and determination of band polarizations in randomly oriented systems with spin $S \geq 1/2$. Applications to $S = 1/2$ and $S = 5/2$. *Inorg. Chem. 38* 1865.
55. Straganz, G. D., and Nidetzky, B. (2005) Reaction coordinate analysis for beta-diketone cleavage by the non-heme Fe2+-dependent dioxygenase Dke1. *J. Am. Chem. Soc. 127*, 12306–12314.
56. Thomson, A. J., and Johnson, M. K. (1980) Magnetization Curves of Hemoproteins Measured by Low-Temperature Magnetic-Circular-Dichroism Spectroscopy. *Biochem. J. 191*, 411–420.
57. Calhoun, J. R., Bell, C. B., 3rd., Smith, T. J., Thamann, T. J., DeGrado, W. F., and Solomon, E. I. (2008) Oxygen Reactivity of the Biferrous Site in the de novo Designed Four Helix Bundle Peptide DFsc: Nature of the "Intermediate" and Reaction Mechanism. *J. Am. Chem. Soc.*, in press.
58. Tong, W., Burdi, D., Riggs-Gelasco, P., Chen, S., Edmondson, D., Huynh, B. H., Stubbe, J., Han, S., Arvai, A., and Tainer, J. (1998) Characterization of Y122F R2 of *Escherichia coli* ribonucleotide reductase by time-resolved physical biochemical methods and X-ray crystallography. *Biochemistry 37*, 5840–5848.
59. Wei, P. P., Skulan, A. J., Mitic, N., Yang, Y. S., Solomon, E. I., Bollinger, J. M., and Saleh, L. (2003) Circular dichroism and magnetic circular dichroism studies of the reduced binuclear nonheme iron sites of D84E and D84E/W48F ribonucleotide reductase mutants. Comparison to reduced methane monooxygenase and contributions to O2 reactivity. *J. Inorg. Biochem. 96*, 250–250.

BI801212F